Bull. Mater. Sci., Vol. 39, No. 4, August 2016, pp. 943–952. © Indian Academy of Sciences.
DOI 10.1007/s12034-016-1225-8

Hydrothermal synthesis, characterization and luminescent properties of lanthanide-doped $NaLaF_4$ nanoparticles

JIGMET LADOL, HEENA KHAJURIA, SONIKA KHAJURIA and HAQ NAWAZ SHEIKH*
Department of Chemistry, University of Jammu, Jammu 180006, India

MS received 16 December 2015; accepted 2 February 2016

Abstract. Nanoparticles of sodium lanthanum (III) fluoride-doped and co-doped with Eu^{3+}/Tb^{3+} were prepared by the hydrothermal method using citric acid as structure-directing agent. Structural aspects and optical properties of synthesized nanoparticles were studied by powder X-ray diffraction (XRPD), scanning electron microscopy (SEM), transmission electron microscopy (TEM), selected area electron diffraction (SAED), energy-dispersive X-ray spectra (EDS), particle size by dynamic light scattering (DLS), Fourier transform infrared (FTIR) spectrum and photoluminescence (PL) techniques. Nanoparticles consist of well-crystallized hexagonal phase and the average crystallite size for undoped and doped-$NaLaF_4$ nanoparticles are in the range of 20–22 nm. TEM images show that nanoparticles have cylindrical shape and crystalline nature of nanoparticles was confirmed by SAED patterns. Down-conversion (DC) luminescent properties of doped $NaLaF_4$ were also investigated and impact of co-doping has been explored.

Keywords. Citric acid; X-ray diffraction; down-conversion emission; energy transfer.

1. Introduction

Lanthanide-doped fluoride nanoparticles have attracted attention due to distinct optical, electrical and magnetic properties arising from 4f electronic configurations [1–3]. Among various host materials of lanthanide-doped fluoride nanoparticles, $AReF_4$ (A = alkali metal; Re = rare-earth metal; F = fluoride) exhibit some distinct advantages relative to other luminescent materials due to the low phonon energy, low non-radiative decay rates and high radiative emission rates [4,5]. These compounds doped with trivalent lanthanide ions possess prominent luminescent features such as high luminescence quantum yield, narrow bandwidth, long-lived emission and large Stokes shift [6,7]. These properties made them promising materials in numerous fields such as solid state lasers [8], multicolour three-dimensional displays [9], optical processing sensors [10], solar cells [11], biological labels and imaging [12]. Due to the concerns of toxicity and optical instability of quantum dots and organic dye molecules used as biomarkers for applications in immunoassay, cell imaging and photodynamic therapy (PDT), lanthanide-doped fluorescent nanoparticles have become promising alternative materials owing to their superior physical and chemical properties [13,14]. Sodium rare-earth fluorides exhibit two polymorphic forms in crystalline structure, namely, cubic and hexagonal phases, depending on the synthetic conditions and methods. Among all the investigated lanthanide-doped nanoscale hosts, the hexagonal phase sodium rare-earth fluorides are considered as the most excellent host lattices for photoluminescence (PL) since they normally have lower phonon energy, which decreases the non-radiative relaxation probability and subsequently increases the luminescent efficiency [15–17]. The radius of rare-earth ions plays a key role in controlling crystal phase and shape. Sodium rare-earth fluoride hosts with large ionic radii, have high tendency to form hexagonal phase nanoparticles [18]. The crystal structure and size of the sodium rare-earth fluorides play important roles in controlling the optical properties [19–21]. These lanthanide-doped luminescent materials have been synthesized using various methods such as thermal decomposition [22], co-precipitation [23], hydro(solvo)thermal [24,25], ionic liquid-based synthesis [26], microemulsion-assisted [27] and microwave-assisted synthesis [28]. Among these methods, hydrothermal synthesis allows excellent control over particle size, shape, distribution and crystallinity of the material. Synthesis is conducted in a stainless autoclave using water as a solvent and nanoparticles formation occurs under high autogenous pressure at a synthetic temperature above the boiling point of solvent or mixed solution.

In this paper, Tb^{3+}, Eu^{3+} and Eu^{3+}/Tb^{3+} co-doped hexagonal phase $NaLaF_4$ nanoparticles have been successfully synthesized by a facile hydrothermal method. Luminescent properties of dopant ion in hexagonal $NaLaF_4$ nanoparticles have been investigated and discussed.

2. Experimental

2.1 *Materials and characterization techniques*

Europium(III) nitrate hexahydrate $Eu(NO_3)_3 \cdot 6H_2O$ (99.9%), terbium(III) nitrate hydrate $Tb(NO_3)_3 \cdot H_2O$ (99.9%) and ammonium tetrafluoroborate NH_4BF_4 were purchased from

---

*Author for correspondence (hnsheikh@rediffmail.com)

Alfa Aesar and other chemicals such as citric acid, sodium hydroxide and ethanol were of analytical grade. All the chemicals were used as received without further purification. Deionized water was used throughout the process.

The phase structure and size of as-prepared samples were determined from powder X-ray diffraction (XRPD) using D8 X-ray diffractometer (Bruker) at a scanning rate of 12° $\min^{-1}$ in the 2θ range from 10 to 80°, with CuKα radiation ($\lambda = 0.15405$ nm). Transmission electron microscopy (TEM) and selected area electron diffraction (SAED) patterns were recorded on Tecnai G^2 S-twin transmission electron microscope with field emission gun operating at 200 kV. Samples for TEM measurements were prepared by evaporating a drop of colloid onto a carbon-coated copper grid. The energy spectra were obtained by energy-dispersive X-ray spectrum (EDS, Oxford Instrument) equipped on scanning electron microscope (SEM, Suprs55Zeiss). SEM provided extremely wide operating voltage range from 0.02 to 30 kV. The particle size of each compound was determined by dynamic light scattering (DLS) technique using Zetasizer Nano ZS-90 (Malvern Instruments Ltd, Worcestershire, UK). The infrared spectra were recorded on a Shimadzu Fourier transform infrared spectrometer (FTIR) over the range of wave number 4000–400 cm^{-1} and the standard KBr pellet technique was employed. The PL excitation and emission spectra were recorded at room temperature using Agilent Cary Eclipse Fluorescence Spectrophotometer equipped with a xenon lamp that was used as an excitation source. Radiative lifetime of luminescent nanospheres was calculated from decay curves using Picosecond Time-resolved Spectrometer, Eddinburg Instruments, Model: FSP920. All the measurements were performed at room temperature.

2.2 *Synthesis of undoped and doped-NaLaF$_4$ nanoparticles*

The pure/undoped NaLaF$_4$ and Ln^{3+} (Ln = Tb, Eu and Eu/Tb)-doped NaLaF$_4$ nanoparticles were synthesized by a facile hydrothermal method using citric acid as the structure-directing agent. In typical synthesis of undoped NaLaF$_4$ nanoparticles, aqueous solution (3.5 ml) of $\text{La(NO}_3)_3{\cdot}6\text{H}_2\text{O}$ (0.5 mmol, 0.22 g) was mixed with aqueous solution (5 ml) of citric acid (0.5 mmol, 0.1 g) and NaOH (0.3 g), while stirring thoroughly. To this reaction mixture, 5 ml of ethanol was added. Then, 1 ml aqueous solution of NH$_4$BF$_4$ (2 mmol, 0.20 g) was added dropwise to the mixture. After vigorous stirring at room temperature for about 30 min, colloidal solution was transferred into a 23 ml Teflon-lined autoclave, sealed and heated at 180°C for 18 h. To synthesize $\text{NaLa}_{0.80}\text{Tb}_{0.20}\text{F}_4$ nanoparticles, aqueous solution (3.5 ml) of $\text{La(NO}_3)_3{\cdot}6\text{H}_2\text{O}$ (0.4 mmol, 0.173 g) and $\text{Tb(NO}_3)_3{\cdot}\text{H}_2\text{O}$ (0.1 mmol, 0.04 g) was mixed with aqueous solution (5 ml) of citric acid (0.5 mmol, 0.1 g) and NaOH (0.3 g), while stirring thoroughly. All reaction conditions and procedures adopted were same as above. As autoclave was cooled to room temperature naturally, the precipitates were separated by centrifugation, washed with deionized water and ethanol in sequence, and then collected nanoparticles were dried at 60°C for 12 h. Similar procedure and reaction condition were used for the synthesis of $\text{NaLa}_{0.80}\text{Eu}_{0.20}\text{F}_4$ and $\text{NaLa}_{0.80}\text{Eu}_{0.10}\text{Tb}_{0.10}\text{F}_4$ nanoparticles.

3. Results and discussion

3.1 *XRPD measurements*

Figure 1 shows the XRPD patterns of undoped NaLaF$_4$ and doped-NaLaF$_4$: Tb^{3+}, NaLaF$_4$: Eu^{3+}, NaLaF$_4$: Eu^{3+}/Tb^{3+} nanoparticles. The crystallinity of these nanoparticles is confirmed by their highly intense X-ray reflections in their corresponding XRPD patterns. In all the cases, width of the diffraction lines is broad which indicates that the size of synthesized NaLaF$_4$ nanoparticles is in nanoscale. The XRPD patterns of the nanoparticles show that the peak positions and intensities agree well with the literature values in the JCPDS standard card (no. 50-0155) for hexagonal phase NaLaF$_4$ nanoparticles. Moreover, no other phase was detected, revealing high purity of samples. Similar patterns of rare-earth-doped NaLaF$_4$ nanoparticles indicate that rare

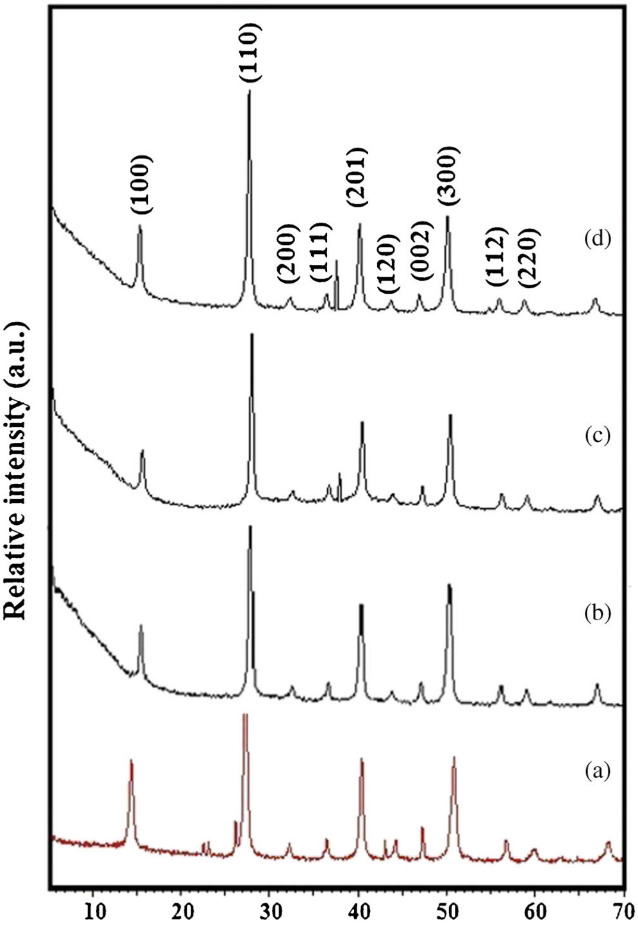

Figure 1. XRPD spectra of (**a**) undoped NaLaF$_4$, (**b**) doped NaLaF$_4$: Tb^{3+}, (**c**) NaLaF$_4$: Eu^{3+} and (**d**) NaLaF$_4$: Eu^{3+}/Tb^{3+} nanoparticles.

earth dopants are occupying La^{3+} site in the lattice and single phase products are obtained even on doping. The hexagonal $NaLaF_4$ phase showing diffraction peaks at 16.6, 28.9, 33.6, 37.7, 41.4, 44.9, 48.1, 51.3, 57.2 and 60.0° can be indexed to the planes (100), (110), (200), (111), (201), (120), (002), (300), (112) and (220), respectively. Major peaks were used to calculate the average crystallite size of these nanoparticles according to Scherrer's equation

$$D = K\lambda/\beta\cos\theta,$$

where D is the crystallite size, λ the wavelength of the CuKα radiant, $\lambda = 0.15405$ nm, β the FWHM (full-width at half-maximum) of diffraction peaks, θ the diffraction angle and K the Scherrer constant equals to 0.89. The calculated average crystallite size of nanoparticles lies in the range of 20–22 nm. Slight variation in particle size is due to dopant ions which cause negligible change in FWHM values. The enhanced intensity of peaks indicates preferential crystal growth in this direction. The average diameters of the three samples calculated by XRPD data and analysed by the DLS technique are summarized in table 1. Various other parameters (table 1) such as interplanar spacing (d in Å), microstrain (ε), dislocation density (ρ in 10^{15} m m^{-3}) and distortion parameter (g) along (110) plane were calculated using the following equations:

$$d = \lambda/2\sin\theta;\ \varepsilon = \beta\cos\theta/4;\ \rho = 1/D^2\ (D \text{ in Å})$$
$$\text{and } g = \beta/\tan\theta.$$

It is clear from the table that microstrain value decreases with increase in the crystallite size [29].

3.2 SEM, TEM and EDS analyses

The surface morphology of the undoped and doped-$NaLaF_4$ nanoparticles was explored from SEMs. SEM images of nanoparticles at different magnifications show hexagonal-shaped $NaLaF_4$ nanostructures (figure 2). Compositional analysis by EDS (figure 3) reveals incorporation of Ln^{3+} (Ln = Tb, Eu and Eu/Tb) ions in host $NaLaF_4$ nanoparticles. Magnesium is present as impurity in figure 3a.

Table 1. Evaluated parameters from XRPD data and DLS analysis for undoped and doped $NaLaF_4$ nanoparticles.

Samples	Peak position, 2θ (degree)	Particle size, D (nm)		d-Value (Å)		Micro-strain, ε	Dislocation density, ρ (10^{15} m m^{-3})	Distortion parameter, g
		PXRD	DLS	Observed	Calculated			
$NaLaF_4$	29.006	20.19	24.0	3.078	3.074	0.0972	2.453	1.552
$NaLaF_4 : Tb^{3+}$	28.996	21.90	49.9	3.059	3.058	0.0895	2.085	1.431
$NaLaF_4 : Eu^{3+}$	29.003	20.79	48.6	3.047	3.046	0.0944	2.314	1.508
$NaLaF_4 : Eu^{3+}/Tb^{3+}$	29.024	21.24	81.2	3.072	3.074	0.0919	2.217	1.468

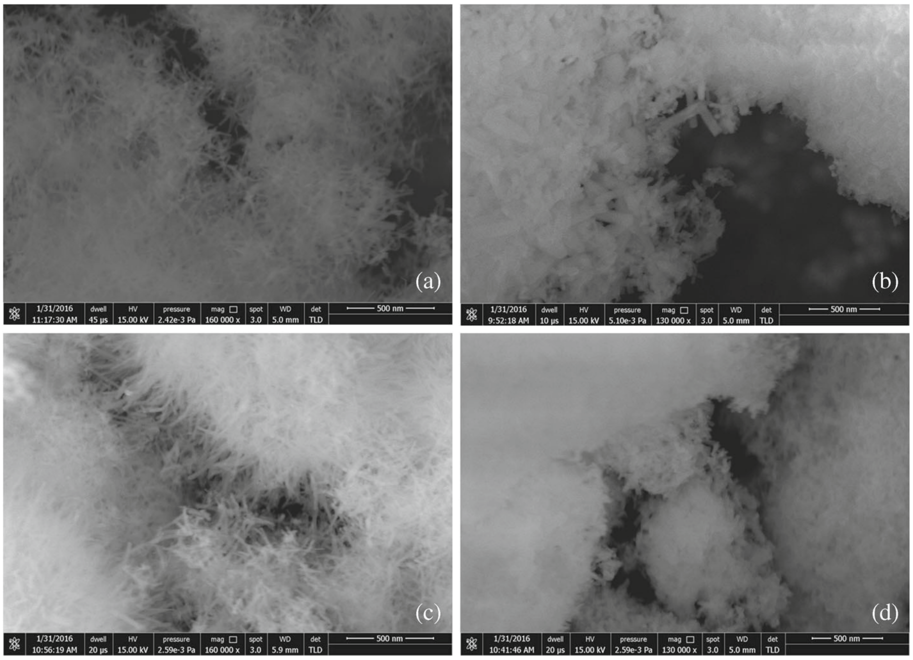

Figure 2. SEM images of (**a**) undoped $NaLaF_4$, (**b**) doped $NaLaF_4 : Tb^{3+}$, (**c**) $NaLaF_4 : Eu^{3+}$ and (**d**) $NaLaF_4 : Eu^{3+}/Tb^{3+}$ nanoparticles.

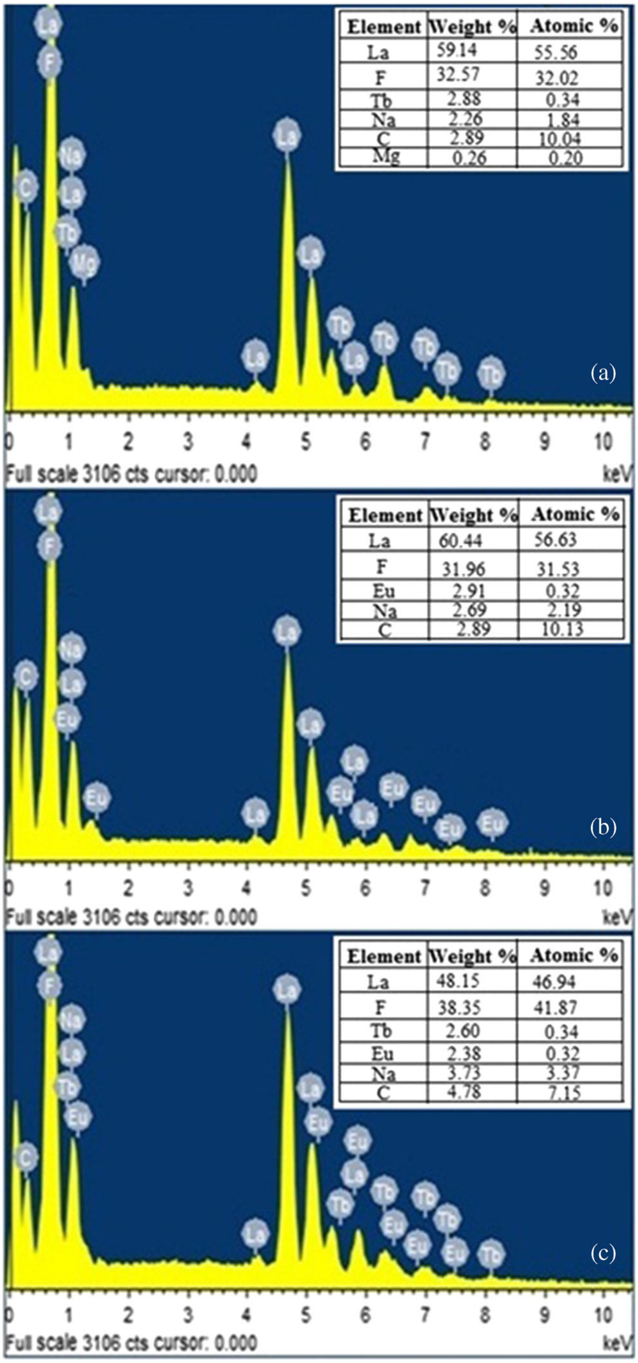

Element	Weight %	Atomic %
La	59.14	55.56
F	32.57	32.02
Tb	2.88	0.34
Na	2.26	1.84
C	2.89	10.04
Mg	0.26	0.20

Element	Weight %	Atomic %
La	60.44	56.63
F	31.96	31.53
Eu	2.91	0.32
Na	2.69	2.19
C	2.89	10.13

Element	Weight %	Atomic %
La	48.15	46.94
F	38.35	41.87
Tb	2.60	0.34
Eu	2.38	0.32
Na	3.73	3.37
C	4.78	7.15

Figure 3. EDS spectra of (**a**) $NaLaF_4 : Tb^{3+}$, (**b**) $NaLaF_4 : Eu^{3+}$ and (**c**) $NaLaF_4 : Eu^{3+}/Tb^{3+}$ nanoparticles.

Figure 4 shows TEM images and SAED patterns of undoped and doped-$NaLaF_4$ nanoparticles. The images show well-dispersed particles cylindrical-shaped morphology at different magnifications. The SAED patterns show that these nanoparticles are well crystalline in nature. High crystallinity is important for phosphors because high crystallinity generally means fewer traps and stronger UC and DC luminescences.

3.3 *Formation mechanism of nanoparticles*

On the basis of the above analysis, growth of nanoparticles of lanthanum fluorides takes place through a series of chemical transformations under the influence of surfactant. It is known that citric acid can be adsorbed strongly on metal and mineral surfaces and significantly alters the surface properties and mineral growth behaviour [30]. Here, citric acid may play a crucial role in the formation of undoped and doped-submicron rods. First, the rare-earth ions react with citrate groups in solution to form the rare-earth citrate complex, equation (1). Then, in aqueous solution, NH_4BF_4 is hydrolysed to produce BO_3^{3-} and F^- anions, as shown in equation (2). Sodium hydroxide in presence of acidic medium produces Na^+ ion and water molecule, equation (3). La^{3+}-cit complex then reacts with F^- ion produced during slow hydrolysis of NH_4BF_4 to form $NaLaF_4$ nuclei as presented in equation (4). The probable reaction processes for the formation of $NaLaF_4$ can be summarized as

$$La^{3+} + \text{citrate} \rightarrow La^{3+} - \text{cit}, \qquad (1)$$

$$BF_4^- + 3H_2O \rightarrow 3HF + F^- + H_3BO_3, \qquad (2)$$

$$NaOH + H^+ \rightarrow Na^+ + H_2O, \qquad (3)$$

$$(La^{3+} - \text{cit}) + 4F^- + Na^+ \rightarrow NaLaF_4 - \text{cit}. \qquad (4)$$

At this stage, the nucleation rate of $NaLaF_4 : Tb^{3+}$, $NaLaF_4 : Eu^{3+}$ and $NaLaF_4 : Eu^{3+}/Tb^{3+}$ nanoparticles is strongly affected by the incorporation of F^- ions into the rare-earth complex [31]. Finally, citrate groups selectively bind to certain crystal surfaces of the nanoparticles, probably providing driving force (electrostatic, hydrogen, coordination bonds, etc.) that makes primary particles assemble into polydispersed submicron rods [32–34].

3.4 *Particle size by DLS*

Figure 5 shows the particle size distribution curves for synthesized Ln^{3+}-doped and undoped $NaLaF_4$ nanoparticles determined by DLS. Before DLS analysis, the nanoparticles were uniformly dispersed in deionized water by mild sonication for 5 min. The approximate sizes of undoped and doped-$NaLaF_4$ nanoparticles were found in the range of 24–81 nm. It was observed that doped-$NaLaF_4$ nanoparticles have larger size when compared to undoped-$NaLaF_4$ nanoparticles. Undoped $NaLaF_4$, La^{3+} has larger ionic radius and large surface electron charge density that hinder the diffusion of F^- ions needed for crystal growth as a result of charge repulsion, consequently resulting in retardation of nanocrystal growth [35]. And in case of doped $NaLaF_4$, where La^{3+} is substituted by dopant ion with smaller ionic radius, increase in size of nanoparticles is attributed to the same reasons. It can be seen that the sizes of the particles analysed using DLS technique are larger than those calculated from the XRPD measurement. This might be due to the surface

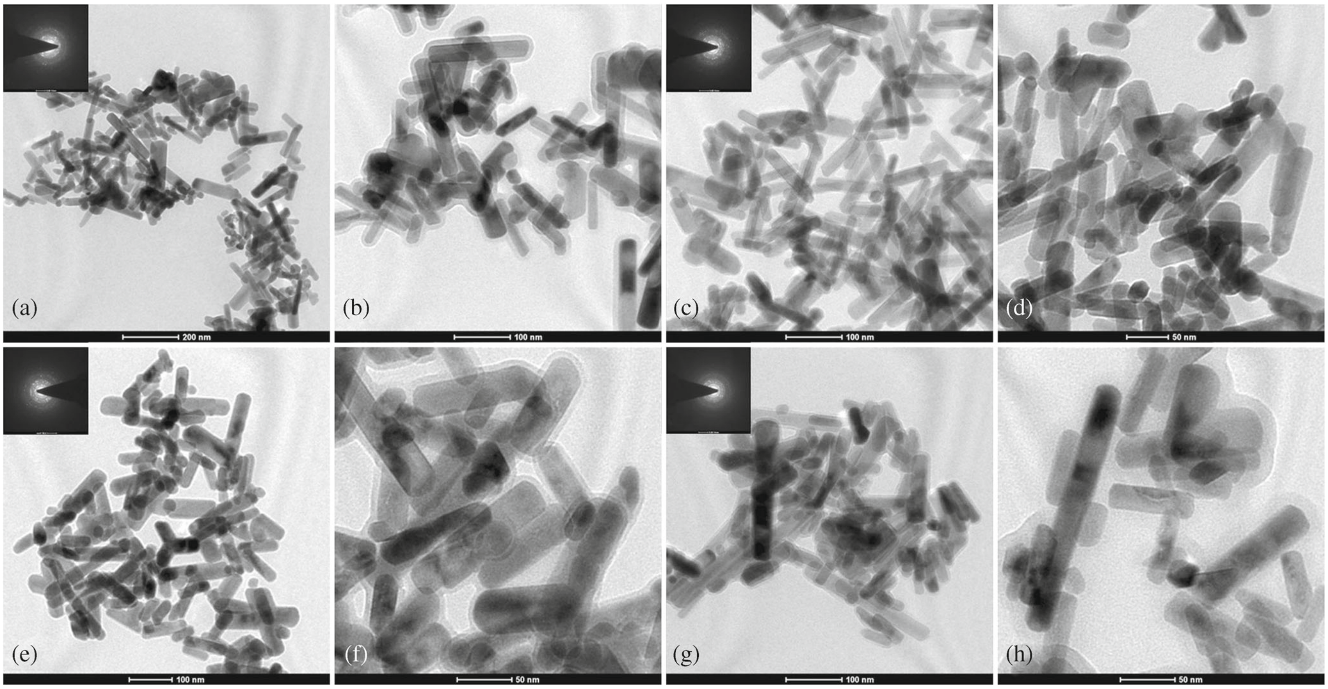

Figure 4. TEM images of (**a**, **b**) undoped NaLaF$_4$; (**c**, **d**) doped NaLaF$_4$: Tb^{3+}; (**e**, **f**) NaLaF$_4$: Eu^{3+} and (**g**, **h**) NaLaF$_4$: Eu^{3+}/Tb^{3+} nanoparticles. Insets in **a**, **c**, **e** and **g** are SAED patterns.

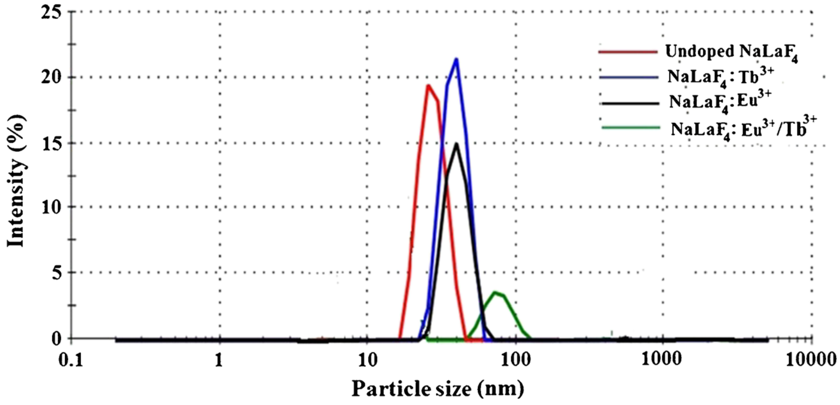

Figure 5. Particle size by DLS for undoped NaLaF$_4$, doped NaLaF$_4$: Tb^{3+}, NaLaF$_4$: Eu^{3+} and NaLaF$_4$: Eu^{3+}/Tb^{3+} nanoparticles.

solvation and agglomeration/aggregation of the particles in the colloidal solution.

3.5 *FTIR spectra*

The presence of citrate ligands at the surface of NaLaF$_4$: Tb^{3+}, NaLaF$_4$: Eu^{3+} and NaLaF$_4$: Eu^{3+}/Tb^{3+} nanoparticles can be proved by FTIR. Figure 6 shows the FTIR spectrum of as-prepared submicron rods. The broad band at 3451 cm^{-1} can be attributed to the stretching mode of hydrogen-bonded hydroxyl groups. The asymmetrical and symmetrical stretching vibration modes of CH$_2$ group appear around 2908 and 2834 cm^{-1}, respectively. The bands at 1686 and 1384 cm^{-1} can be assigned to the asymmetric and symmetric stretching vibrations of the carboxylic group (–COOH) in the coated-citric acid, respectively.

3.6 *Luminescence properties*

One of the most remarkable features of lanthanide compounds is PL. The lanthanide ions have electronic configuration (Xe) 4f^n (n = 0–14) that generates abundant electronic levels. Luminescence of lanthanide ions essentially originates from transitions of partially filled 4f electrons [36,37]. Since 4f orbitals are shielded by filled 5s^2 5p^6 sub-shells, the emission bands remain narrow even at room temperature.

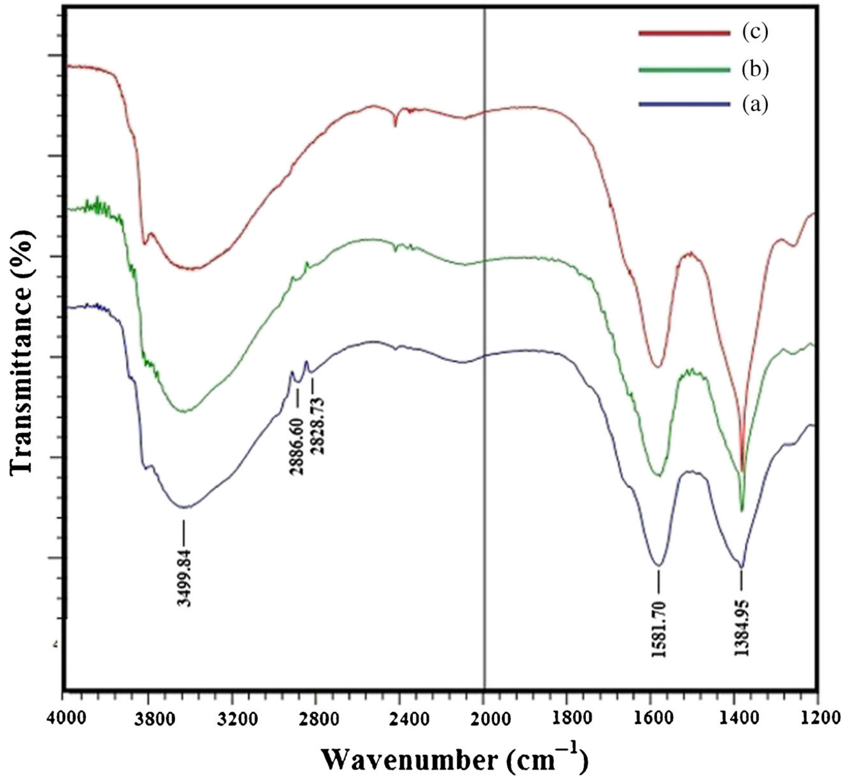

Figure 6. FTIR spectra of (**a**) $NaLaF_4 : Tb^{3+}$, (**b**) $NaLaF_4 : Eu^{3+}$ and (**c**) $NaLaF_4 : Eu^{3+}/Tb^{3+}$ nanoparticles.

As a consequence of this, lanthanide-doped nanoparticles are able to emit light that covers ultraviolet (UV)–Visible to near infrared (NIR) regions. Our experimental results and previous investigations reveal that $NaLaF_4$ is a promising host lattice for doping optically active lanthanide ions [38]. Accordingly, it was mainly focussed on down-conversion luminescent properties of Ln^{3+} (Ln = Tb, Eu and Eu/Tb)-doped $NaLaF_4$ nanoparticles. Eu^{3+} and Tb^{3+} were chosen as dopant ions as these metal ions are highly luminescent with relatively long lifetimes [39].

3.6a $NaLaF_4$: Tb^{3+}: Figure 7 shows the solid-state excitation and emission spectra for the $NaLaF_4 : 20\%\ Tb^{3+}$ sample. The excitation spectrum (black line) is composed of characteristic f–f transition lines within the Tb 4f configuration, which can be assigned to the transitions from the $^7F_6$ ground state to the different excited states of Tb^{3+}, i.e., 283 nm ($^5I_6$), 303 nm ($^5H_6$), 318 nm ($^5D_0$), 339 nm ($^5G_2$), 351 nm ($^5D_2$) and 368 nm ($^5G_6$). Upon excitation at 351 or 377 nm, the obtained emission spectrum consists of four obvious lines centred at 490, 545, 585 and 621 nm originating from the

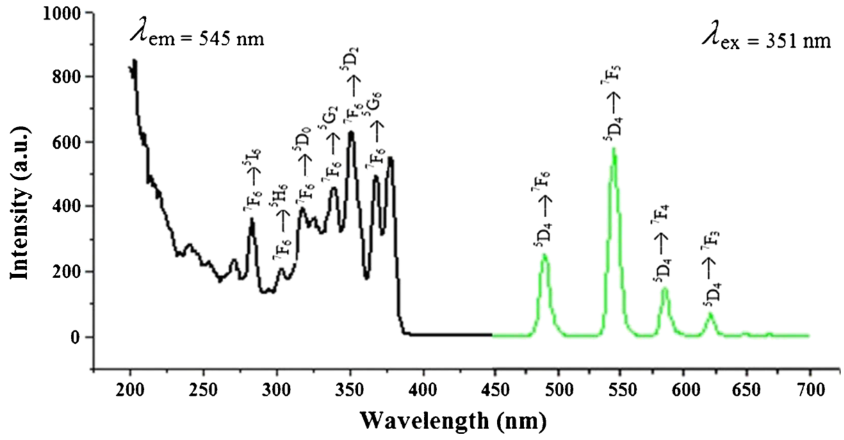

Figure 7. (Colour online) Excitation (black lines) and emission spectra (green lines) of $NaLaF_4 : 20\%\ Tb^{3+}$ nanoparticles.

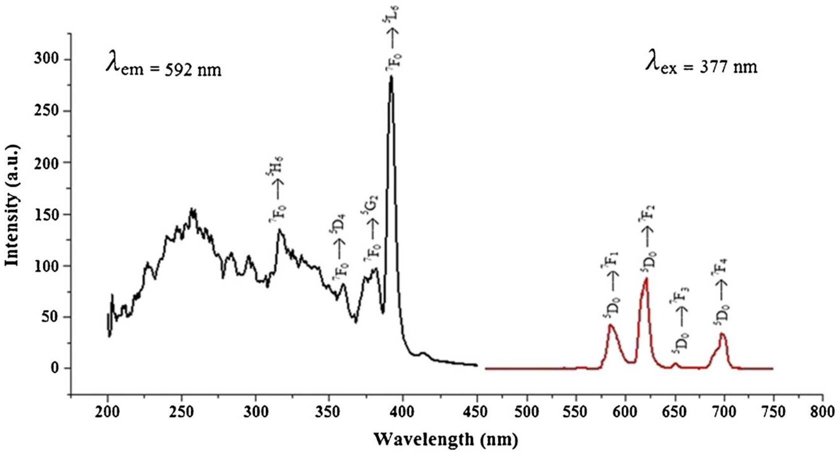

Figure 8. (Colour online) Excitation (black lines) and emission spectra (red lines) of $NaLaF_4$: 20% Eu^{3+} nanoparticles.

transitions from the $^5D_4$ excited state to the ^7F_J ($J = 6, 5, 4, 3$) ground states of the Tb^{3+} ions. The transition at 545 nm, i.e., $^5D_4 \rightarrow {}^7F_5$ is most intense peak as it corresponds to transition, i.e., both magnetic dipole and electric-dipole allowed [40].

3.6b $NaLaF_4$: Eu^{3+}: The excitation and emission spectra for $NaLaF_4$: 20% Eu^{3+} sample are shown in figure 8. The excitation spectrum (black line) consists of several characteristic excitation lines of Eu^{3+} originating from its $4f^6$ configuration, which can be clearly assigned as 317 nm: $^7F_0 \rightarrow {}^5H_6$; 361 nm: $^7F_0 \rightarrow {}^5D_4$; 377 nm: $^7F_0 \rightarrow {}^5G_2$; and 393 nm: $^7F_0 \rightarrow {}^5L_6$. Upon excitation at 377 nm, the corresponding emission spectrum comprises emission lines assigned at 592 nm: $^5D_0 \rightarrow {}^7F_1$; 615 nm: $^5D_0 \rightarrow {}^7F_2$; 650 nm: $^5D_0 \rightarrow {}^7F_3$ and 695 nm: $^5D_0 \rightarrow {}^7F_4$. Experimental data on photophysical properties of a number of Eu^{3+} ions established that the emission band centred around 592 nm corresponding to the $^5D_0 \rightarrow {}^7F_1$ transition is magnetic dipole in character, whereas the emission band centred around 615 and 695 nm corresponding to the $^5D_0 \rightarrow {}^7F_2$, $^5D_0 \rightarrow {}^7F_4$ transitions, respectively, are electric dipole in character [41]. The transitions to the $^7F_{0,3,5}$ levels are forbidden both in magnetic and electric dipole schemes and are usually very weak in the emission spectrum. The emission spectrum of Eu^{3+} ion is strongly influenced by the symmetry of the environment. If Eu^{3+} occupies a crystal site with inversion symmetry, the electric dipole transitions are strictly forbidden and $^5D_0 \rightarrow {}^7F_1$ is usually the dominant emission line. If there is no inversion symmetry at the Eu^{3+} site, the strength of the electric dipole transitions is higher. The $^5D_0 \rightarrow {}^7F_2$ transition is usually the strongest emission line in this case, because transitions with $\Delta J = \pm 2, \pm 4$ are hypersensitive to small deviations from inversion symmetry [42].

3.6c $NaLaF_4$: Eu^{3+}/Tb^{3+}: Figure 9a and b shows the excitation and emission spectra for co-doped (10% Eu^{3+} and 10% Tb^{3+}) $NaLaF_4$ nanoparticles. The excitation spectrum consists of characteristic f–f transition lines of both Tb^{3+} and Eu^{3+} ions which can be clearly assigned as 317 nm:

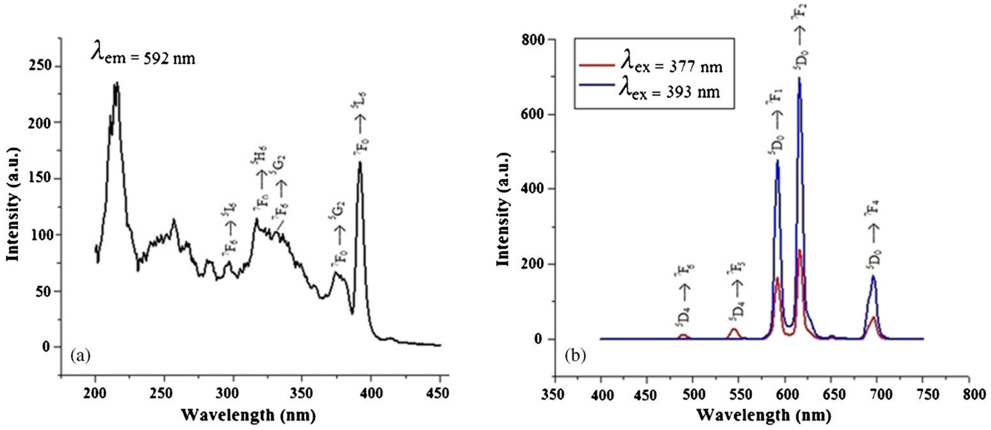

Figure 9. (**a**) Excitation and (**b**) emission spectra of $NaLaF_4$: 10% Eu^{3+}/Tb^{3+} nanoparticles monitored at 377 and 393 nm, respectively.

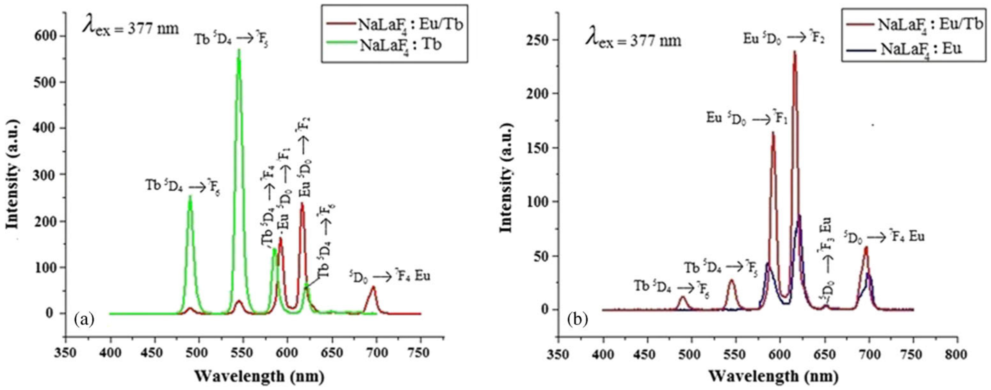

Figure 10. Emission spectra of (**a**) Tb^{3+} and Eu^{3+}/Tb^{3+} co-doped $NaLaF_4$ nanoparticles and (**b**) Eu^{3+} and Eu^{3+}/Tb^{3+} co-doped $NaLaF_4$ nanoparticles monitored at 377 nm. Here, the decreased $^5D_4$ to $^7F_{6,5}$ transitions in Tb as well as the increase in Eu transitions are more evident.

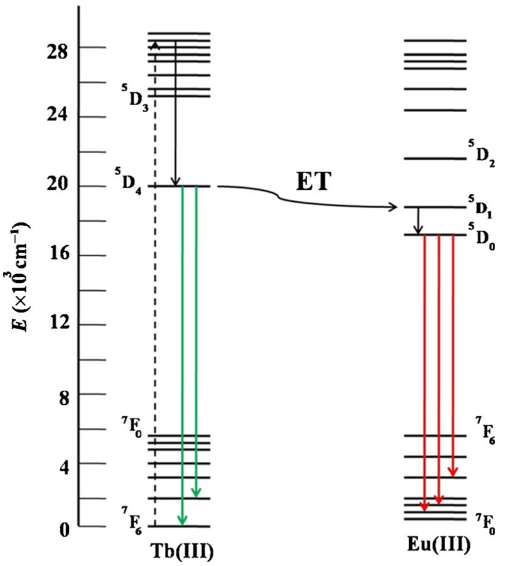

Figure 11. Energy level diagram showing energy transfer between Tb^{3+} and Eu^{3+} ion.

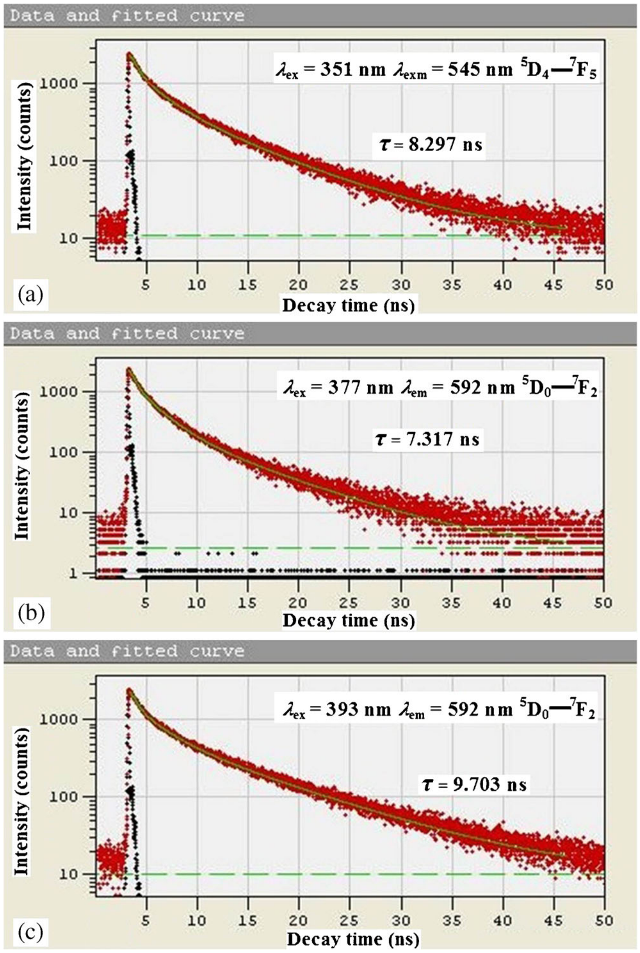

Figure 12. Decay curves of (**a**) Tb^{3+} in $NaLaF_4 : Tb^{3+}$, (**b**) Eu^{3+} in $NaLaF_4 : Eu^{3+}$ and (**c**) Eu^{3+} in $NaLaF_4 : Eu^{3+}/Tb^{3+}$ nanoparticles.

$^7F_0 \rightarrow {}^5H_6$ (Eu); 283 nm: $^7F_6 \rightarrow {}^5I_6$ (Tb); 339 nm: $^7F_6 \rightarrow {}^5G_2$ (Tb); 377 nm: $^7F_0 \rightarrow {}^5G_2$ (Eu); and 393 nm: $^7F_0 \rightarrow {}^5L_6$ (Eu). When excited at 377 nm, the corresponding emission spectrum comprises emission lines originating from both Tb^{3+} and Eu^{3+} ions. These lines are assigned at 490 nm: $^5D_4 \rightarrow {}^7F_6$ (Tb); 545 nm: $^5D_4 \rightarrow {}^7F_5$ (Tb); 592 nm: $^5D_0 \rightarrow {}^7F_1$(Eu); 615 nm: $^5D_0 \rightarrow {}^7F_2$ (Eu); and 695 nm: $^5D_0 \rightarrow {}^7F_4$(Eu). Emission spectrum shows only two emission lines with diminished intensity (out of characteristic four lines) of Tb^{3+} and only three emission lines with moderate intensity (out of characteristic four lines) of Eu^{3+}. Upon excitation at 393 nm, only emission lines originating from Eu^{3+} ion appear, whereas emission from Tb^{3+} is completely quenched. Figure 10a shows emission spectra of Tb^{3+}-doped $NaLaF_4$ and Eu^{3+}/Tb^{3+} co-doped $NaLaF_4$ nanoparticles when excited at 377 nm. It is seen that characteristic emission from Tb^{3+} gets significantly quenched in Tb^{3+}/Eu^{3+} co-doped $NaLaF_4$ nanoparticles as compared to Tb^{3+}-doped nanoparticles. This suppression in intensity of Tb^{3+} emission lines is accompanied by concomitant enhancement in intensity of Eu^{3+} emission lines in Eu^{3+}/Tb^{3+} co-doped

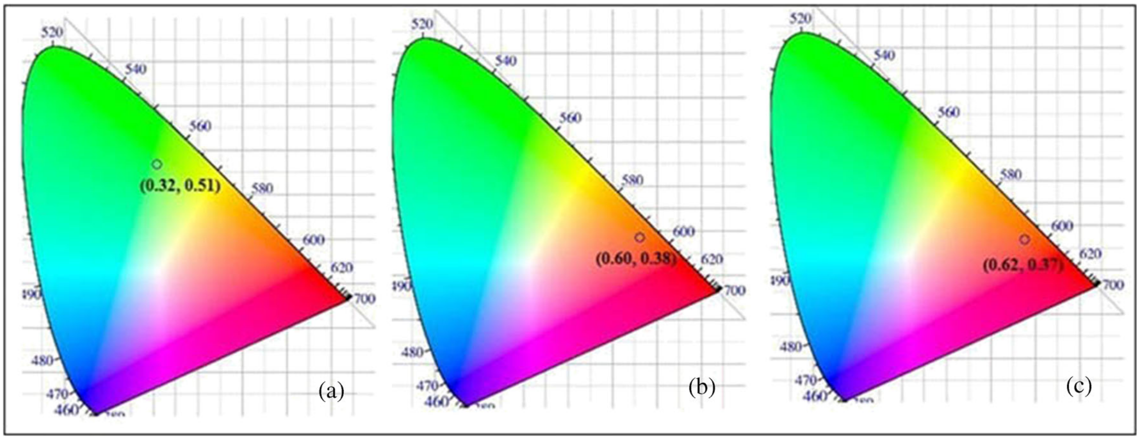

Figure 13. CIE chromatogram for (**a**) NaLaF$_4$: Tb^{3+}, (**b**) NaLaF$_4$: Eu^{3+} and (**c**) NaLaF$_4$: Eu^{3+}/Tb^{3+} nanoparticles.

NaLaF$_4$ nanoparticles. This is further confirmed by comparison of intensity of emission lines in Eu^{3+}-doped NaLaF$_4$ and Eu^{3+}/Tb^{3+} co-doped NaLaF$_4$ nanoparticles (figure 10b). All these experimental observations indicate energy transfer from Tb^{3+} to Eu^{3+} when excited at 377 nm. Thus, Eu^{3+}/Tb^{3+} co-doped NaLaF$_4$ nanoparticles are much better phosphors than Eu^{3+}-doped NaLaF$_4$ nanoparticles, but less phosphor than Tb^{3+}-doped NaLaF$_4$ nanoparticles. The schematic diagram for non-radiative energy transfer process from Tb^{3+} to Eu^{3+}is shown in figure 11. Thus, energy transfer from one lanthanide ion can be used to enhance the luminescence of the other lanthanide ion.

The luminescence decay curves of Tb^{3+} in NaLaF$_4$: Tb^{3+} (figure 12a), Eu^{3+} in NaLaF$_4$: Eu^{3+} (figure 12b) and NaLaF$_4$: Eu^{3+}/Tb^{3+} (figure 12c) can be well fitted into a single exponential function as $I_{(t)} = I_0 \exp(-t/\tau)$ (I_0 is the initial emission intensity at $t = 0$ and τ the lifetime of the emission centre). The lifetime of Tb^{3+} in NaLaF$_4$: Tb^{3+} nanoparticles is 8.297 ns and that of Eu^{3+} in NaLaF$_4$: Eu^{3+} and NaLaF$_4$: Eu^{3+}/Tb^{3+} nanoparticles are 7.317 and 9.703 ns, respectively, as shown in figure 13a–c. Increase in the value of luminescence lifetime for Eu^{3+}/Tb^{3+} co-doped NaLaF$_4$: Eu^{3+}/Tb^{3+} nanoparticles proves the highly efficient energy transfer process occurring from Tb^{3+} to Eu^{3+} relative to that in NaLaF$_4$: Eu^{3+} and NaLaF$_4$: Tb^{3+} nanoparticles. The emission intensity and radiative life time are sensitive to crystal structure and hexagonal phase has been found to give intense emission with longer life time [43].

3.7 *Commission International De I'Eclairage (CIE) coordinates*

The chromaticity coordinates of doped-NaLaF$_4$ nanoparticles have been calculated from the emission spectra by using the CIE system. Figure 13a shows the CIE chromaticity diagram for NaLaF$_4$: Tb^{3+} nanoparticles upon excitation at 351 nm, whereas figure 13b and c shows the same for NaLaF$_4$: Eu^{3+} and NaLaF$_4$: Eu^{3+}/Tb^{3+} nanoparticles, respectively, upon excitation at 377 nm. The CIE coordinate is found (0.32, 0.51) for Tb^{3+}-doped NaLaF$_4$ nanoparticles emitting green light, whereas it is (0.60, 0.38) and (0.62, 0.37) for NaLaF$_4$: Eu^{3+} and NaLaF$_4$: Eu^{3+}/Tb^{3+} nanoparticles, respectively, emitting red light. These results indicate very favourable luminescent features of these nanoparticles.

4. Conclusion

Hexagonal phase undoped and doped-NaLaF$_4$ submicron rods have been synthesized via a simple hydrothermal route by employing NH$_4$BF$_4$ as fluoride source and citric acid as the structure-directing agent. The phase and morphology evolution process as well as the formation mechanism were discussed. XRPD and DLS analyses confirmed the size of particles in the nanometric range. PL studies suggest a general route for the development of highly efficient luminescent DC phosphors in a broad colour range, which have potential application in diverse fields. Purity in colour of nanoparticles is confirmed by means of colour coordinates. This synthetic procedure is facile, environmentally friendly and may be extended to prepare other materials with submicron morphology.

Acknowledgements

We would like to acknowledge Indian Institute of Technology Roorkee and Indian Institute of Technology Guwahati for their technical support. We also thank School of Physics, Shri Mata Vaishno Devi University (SMVDU) for photoluminescence studies.

References

[1] Huang X, Han S, Huang W and Liu X 2013 *Chem. Soc. Rev.* **42** 173

[2] Bunzli J C G, Comby S, Chauvin A S and Vandevyver C D B 2007 *J. Rare Earths* **25** 257

[3] Mahalingam V, Mangiarini F, Vetrone F, Venkatramu V, Bettinelli M, Speghini A *et al* 2008 *J. Phys. Chem.* **112** 17745

[4] Kumar G A, Chen C W, Ballato J and Riman R E 2007 *J. Mater. Chem.* **19** 1523

[5] Liu H, Wang H, Zang X and Chen D 2009 *J. Mater. Chem.* **19** 489

[6] Evanics F, Diamente P R, van Veggel F C, Stanisz G J and Prosser R S 2006 *J. Mater. Chem.* **8** 2499

[7] Kumar R, Nyk M, Ohulchanskyy T Y, Flask C A and Prasad P N 2009 *Adv. Funct. Mater.* **19** 853

[8] Auzel F 2004 *Chem. Rev.* **104** 139

[9] Downing E, Hesselink L, Ralston J and Macfarlane R 1996 *Science* **273** 1185

[10] Jacinto C, Vermelho M, Gouveia E, de Araujo M, Udo P, Astrath N *et al* 2007 *Appl. Phys. Lett.* **91** 071102

[11] van der Ende B M, Aarts L and Meijerink A 2009 *Phys. Chem. Chem. Phys.* **11** 11081

[12] Nyk M, Kumar R, Ohulchanskyy T Y, Bergy E J and Prasad P N 2008 *Nano Lett.* **8** 3834

[13] Qin X, Yokomori T and Ju Y G 2007 *Appl. Phys. Lett.* **90** 073104

[14] Shan J S and Ju Y G 2007 *Appl. Phys. Lett.* **91** 123103

[15] Kramer K W, Biner D, Frei G, Gudel H U, Hehlen M P and Luthi S R 2004 *Chem. Mater.* **16** 1244

[16] Li C, Yang J, Yang P, Lian H and Lin J 2008 *Chem. Mater.* **20** 4317

[17] Xia Z G and Du P 2010 *J. Mater. Res.* **25** 2035

[18] Zeng S J, Ren G Z, Xu C F and Yang Q B 2011 *Cryst. Eng. Comm.* **13** 4276

[19] Ghosh P and Patra A 2008 *J. Phys. Chem.* **112** 19283

[20] Ghosh P and Patra A 2008 *J. Phys. Chem.* **112** 3223

[21] Ghosh P, Kar A and Patra A K 2010 *J. Phys. Chem. C* **114** 715

[22] Chen G Y, Ohulchanskyy T Y, Kachynski A, Agren H and Prasad P N 2011 *AC Nano* **5** 4981

[23] Teng X, Zhu Y, Wei W, Wang S, Huang J, Naccache R *et al* 2012 *J. Am. Chem. Soc.* **134** 8340

[24] Shang M, Li G, Kang X, Yang D, Geng D, Peng C *et al* 2012 *Dalton Trans.* **41** 5571

[25] Shang M M, Geng D L, Kang X J, Yang D M, Zhang Y and Lin J 2012 *Inorg. Chem.* **51** 11106

[26] He M, Huang P, Zhang C L, Hu H Y, Bao C C, Gao G *et al* 2011 *Adv. Funct. Mater.* **21** 4470

[27] Zhou J, Zhu X J, Chen M, Sun Y and Li F Y 2012 *Biomaterials* **33** 6201

[28] Li F, Li C, Liu X, Chen Y, Bai T, Wang L *et al* 2012 *Chem. Eur. J.* **18** 11641

[29] Dawer A L, Shishodia P K, Chouhan J, Kumar G and Mathur A 1990 *Mater. Sci. Lett.* **9** 547

[30] Tian Z R, Voigt J A, Liu J, Mckenzie B, Mcdermott M J, Rodriguez M A *et al* 2003 *Nat. Mater.* **2** 821

[31] Sun Y J, Chen Y, Tian L J, Yu Y, Kong X G, Zhao J W *et al* 2007 *Nanotechnology* **18** 275609

[32] Whitesides G M and Grzybowski B 2002 *Science* **295** 2418

[33] Wang Z L, Hao J H and Chan H L W 2010 *Cryst. Eng. Comm.* **12** 1373

[34] Zhao J W, Sun Y J, Kong X G, Tian L J, Wang Y, Tu L P *et al* 2008 *J. Phys. Chem.* **112** 15666

[35] Wang F, Han Y, Lim C, Lu Y, Wang J, Xu J *et al* 2010 *Nature* **463** 1061

[36] Eliseevaa S V and Bunzli J C G 2010 *Chem. Soc. Rev.* **39** 189

[37] Bunzli J C G and Piguet C 2005 *Chem. Soc. Rev.* **34** 1048

[38] Guangshun Y, Lee W B and Chow G M 2007 *J. Nanosci. Nanotechnol.* **7** 2790

[39] Binnemans K 2009 *Chem. Soc. Rev.* **109** 4283

[40] Gaft M H, Reisfeld R and Panczer G 2005 *Luminescence spectroscopy of minerals and materials,* 2nd edn (Berlin, Heidelberg: Springer)

[41] Kirby A F, Foster D and Richardson F S 1983 *Chem. Phys. Lett.* **95** 507

[42] Kirby A F and Richardson F S 1983 *J. Phys. Chem.* **87** 2544

[43] Ghosh P and Patra A 2008 *J. Phys. Chem. C* **112** 19283; **112** 3223